Available online at www.sciencedirect.com
ScienceDirect
Journal of Computational Physics 225 (2007) 935–948
JOURNAL OF COMPUTATIONAL PHYSICS
www.elsevier.com/locate/jcp

Application of the parabolic spline method (PSM) to a multi-dimensional conservative semi-Lagrangian transport scheme (SLICE) ☆

M. Zerroukat *, N. Wood, A. Staniforth

Met Office, FitzRoy Road, Exeter EX1 3PB, UK

Received 13 September 2006; received in revised form 5 January 2007; accepted 6 January 2007
Available online 19 January 2007

Abstract

The recently devised one-dimensional parabolic spline method (PSM) for efficient, conservative, and monotonic remapping is introduced into the semi-Lagrangian inherently-conserving and efficient (SLICE) scheme for transport problems in multi-dimensions. To ensure mass conservation, an integral form of the transport equation is used rather than the differential form of classical semi-Lagrangian schemes. Integrals within the SLICE scheme are computed using multiple sweeps of PSM along flow-dependent cascade directions to avoid the large timestep-dependent splitting errors associated with traditional fixed-direction splitting. Accuracy of the overall scheme, including at large timestep, is demonstrated using two-dimensional test problems in both Cartesian and spherical geometries and compared with that of the piecewise parabolic method (PPM) applied within the same SLICE framework.
Crown Copyright © 2007 Published by Elsevier Inc. All rights reserved.

AMS: 65M99; 76M25

Keywords: Advection; Cascade; Conservation; Monotonicity; PPM; Remapping

1. Introduction

Semi-Lagrangian (SL) schemes [1] are widely used in atmospheric modelling due to their improved stability compared to their Eulerian counterparts, and to the substantial computational savings concomitant with using large timesteps. However, unlike some Eulerian schemes, the lack of mass conservation with SL schemes can be problematic for relatively long-time integrations, such as those for climate studies [2].

The lack of formal mass conservation in SL schemes has been dealt with by either: (i) applying a posteriori corrections, whereby the original global mass is restored by redistributing the deficit/surplus to minimally change the solution [3] (similar approaches have also been used for non-conservative Eulerian schemes [4]);

☆ © British Crown copyright

* Corresponding author.
E-mail address: mohamed.zerroukat@metoffice.gov.uk (M. Zerroukat).

0021-9991/$ - see front matter Crown Copyright © 2007 Published by Elsevier Inc. All rights reserved.
doi:10.1016/j.jcp.2007.01.006

or (ii) using inherently conserving schemes, whereby the conservation constraint is an integral part of the scheme, i.e. conservative remapping [5–16]. Such schemes are finite/control-volume methods, in that they are all based on estimating integrals of the conserved quantity over a deformed Lagrangian volume (see Section 2 for details). Recently, Lauritzen [17] has given an analysis of some of these schemes.

Although inherently conservative SL schemes are mathematically well formulated, they tend to be more expensive and difficult to generalise to higher dimensions without a substantial increase in computational cost. Therefore, much of the research in this area has been centered on how to remap a multi-dimensional field in an efficient way to allow the flexibility of using higher-order schemes but without a prohibitive computational overhead. To overcome these conflicting criteria, SLICE [18,19] combines a piecewise cubic method (PCM), which is a higher-order alternative to the popular piecewise parabolic method (PPM [20]), with the cascade (flow-dependent decomposition) approach [21]. Building on the previous development of this scheme, a more efficient variant of SLICE, based on the parabolic spline method (PSM) [22], is presented herein. An advantage of PSM is that of all piecewise parabolic functions that satisfy a given mass (average density) distribution, such as the one used by PPM, PSM is an optimal reconstruction since it possesses the minimum norm (or curvature) and best approximation properties [22]. Furthermore, an operation count shows that PSM is 60% more efficient than PPM, and its monotonic filter damps less than PPM's.

The purpose of the present work is to: (i) outline how the one-dimensional (1D) PSM algorithm (and also the PPM algorithm) can be exploited in multi-dimensions using the SLICE cascade directional decomposition strategy; and (ii) demonstrate that PSM's 1D accuracy advantages over PPM also hold for typical 2D test problems of the literature in both Cartesian and spherical geometries.

The rest of the paper is organised as follows: Section 2 outlines the strategy for incorporating the 1D PSM [22] and PPM [20] remappings into the SLICE cascade framework; in Section 3 results of several illustrative tests in Cartesian and spherical geometry are given; and conclusions are summarised in Section 4.

2. 2D remapping with SLICE

This section briefly outlines how the 1D PSM [22] and PPM [20] remappings can be efficiently incorporated into a general strategy to solve higher dimensional (here 2D) problems by using the SLICE methodology [18,19].

2.1. 2D advective transport

Consider (see e.g. [11]) passive 2D advective transport of a scalar quantity ρ governed, in the absence of sources and sinks, by

$$\frac{\partial \rho}{\partial t} + \nabla \cdot (\rho \mathbf{u}) = 0, \tag{2.1}$$

where ρ is the density (amount of scalar per unit volume) of the transported quantity, and $\mathbf{u}$ and t are the transporting velocity field and time, respectively. Let $\delta\mathscr{V}$ be a material volume (strictly an area here as only two dimensions are considered) that moves with the fluid. Then an equivalent integral form of the conservation equation (2.1) is

$$\frac{\mathrm{D}}{\mathrm{D}t}\left(\int_{\delta\mathscr{V}} \rho \, \mathrm{d}\mathscr{V}\right) = 0, \tag{2.2}$$

where $\mathrm{D}/\mathrm{D}t$ is the total derivative following the fluid. Integrating (2.2) from time t_0 to time t_1 gives

$$M_1 = M_0, \tag{2.3}$$

where $M_1 \equiv \int_{\delta\mathscr{V}_1} \rho \, \mathrm{d}\mathscr{V}$, $M_0 \equiv \int_{\delta\mathscr{V}_0} \rho \, \mathrm{d}\mathscr{V}$, and $\delta\mathscr{V}_1$ is the fluid volume at time t_1 that corresponds to the volume $\delta\mathscr{V}_0$ at time t_0. Now let $\delta\mathscr{V}_1$ be a known grid volume, fixed in time, with $\overline{\rho}_1$ being the associated value of the scalar averaged over this volume, so that $M_1 = \overline{\rho}_1 \delta\mathscr{V}_1$. In this context $\delta\mathscr{V}_1$ is then an Eulerian control volume (ECV) whereas $\delta\mathscr{V}_0$ is its corresponding Lagrangian control volume (LCV). Then the problem simplifies to computing the discrete integral M_0, which is a remapping of a given average field $\bar{\rho}$ at time t_0 on regular ECV's to irregular LCV's.

2.2. Cascading with SLICE

SLICE [18,19] exploits the cascade directional decomposition strategy first introduced in [21]. Referring to Fig. 1, the SLICE strategy is now briefly reviewed for Cartesian geometry.

2.2.1. Eulerian and Lagrangian control volumes

Define ECV's (e.g. the rectangle "abcd" in Fig. 1) to be the cells of a regular Eulerian mesh such that $\mathrm{ECV}_{i,j} \equiv [x_{i-1/2}, x_{j+1/2}] \otimes [y_{j-1/2}, y_{j+1/2}]$, with corners denoted by open (red) circles. The centers of ECV's, denoted by solid (red) circles, are located at the intersection of centered Eulerian (continuous thin red) lines x_i and y_j, where $x_i \equiv (x_{i-1/2} + x_{i+1/2})/2$, $y_j \equiv (y_{j-1/2} + x_{j+1/2})/2$.

The locations of the corners of the associated $\mathrm{LCV}_{i,j}$'s (e.g. the quadrilateral "ABCD" in Fig. 1), denoted by open (blue) squares, are determined by a second-order-accurate backwards integration in time (from time t_1 to time t_0) of the trajectory equation

$$\frac{\mathrm{D}\mathbf{x}}{\mathrm{D}t} = \mathbf{u}, \tag{2.4}$$

where $\mathbf{x}$ is 2D position vector [18,19]. The union of all LCV's defines a Lagrangian mesh comprised of bounding Lagrangian lines $X_{i-1/2}$, $X_{i+1/2}$, $Y_{j-1/2}$ and $Y_{j+1/2}$, which are denoted by continuous (blue) thick lines. The intersection points, denoted by open (red) triangles, of bounding Lagrangian lines $X_{i-1/2}$ with Eulerian center lines y_j can then be computed. Centered Lagrangian (dashed blue) lines then connect the midpoints (solid blue squares) of adjacent bounding Lagrangian (solid blue) lines $Y_{j-1/2}$ to one another in a piecewise manner.

The 2D remapping is achieved through multiple sweeps of a 1D remapping algorithm (herein either PSM [22] or PPM [20]): first along the centered Eulerian lines y_j of aligned ECV's, then along the centered Lagrangian lines X_i of aligned LCV's.

2.2.2. 1st cascade

The first cascade, performed along centered Eulerian y_j lines, remaps mass from ECV's to intermediate ECV's (IECV's). These IECV's are (from a visualisation perspective – see Fig. 1) bounded in the y direction by $y_{j-1/2}$ and $y_{j+1/2}$, and bounded in the x direction by Eulerian lines that are parallel to the y axis and

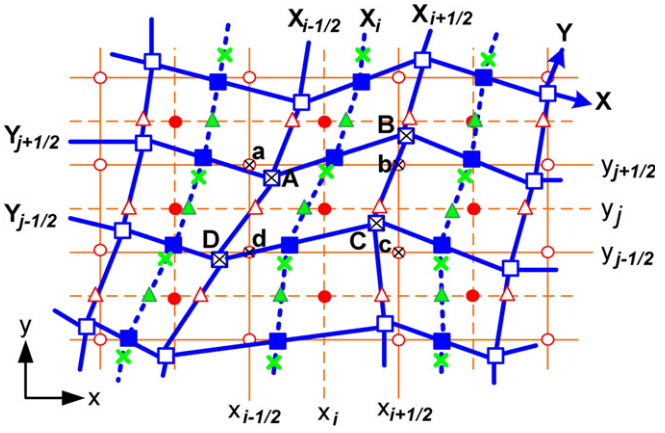

Fig. 1. Superposition of Eulerian (x, y) and Lagrangian (X, Y) grids. Centers of ECV's, where data are held, are denoted by solid (red) circles and corners by open (red) circles; bounding lines $x_{i-1/2}$ and $y_{j-1/2}$ of ECV's by continuous thin (red) lines; centered Eulerian lines x_i and y_j by dashed thin (red) lines; corners of LCV's by open (blue) squares; bounding Lagrangian lines $X_{i-1/2}$ and $Y_{j-1/2}$ of LCV's by continuous thick (blue) lines; midpoints of bounding Lagrangian lines $Y_{j-1/2}$ by solid (blue) squares; centered Lagrangian lines X_i by thick dashed (blue) lines; intersections of Lagrangian lines $X_{i-1/2}$ with Eulerian lines y_j by open (red) triangles; and intersections of centered Lagrangian lines X_i with centered Eulerian lines y_j by solid (green) triangles. Corners of $\mathrm{ECV}_{i,j}$ and $\mathrm{LCV}_{i,j}$ (the departure volume of $\mathrm{ECV}_{i,j}$) are labelled "abcd" and "ABCD", respectively; and shown as open crossed circles and squares respectively. Note however that "abcd" and "ABCD" do not overlap, as they do in this schematic, when the local Courant number is greater than unity.

that pass through the intersection points (denoted by open (red) triangles) of bounding Lagrangian lines $X_{i-1/2}$ with Eulerian center lines y_j. Since the width $\Delta y_j \equiv y_{j+1/2} - y_{j-1/2}$ of these IECV's remains constant along y_j, the 1D PSM [22] or PPM [20] algorithms are used to remap mass from the original ECV's to the IECV's.

2.2.3. 2nd cascade

The mass of each IECV, now known, is considered to be a point mass concentrated at the intersection points (denoted by solid (green) triangles) of a centered Lagrangian line X_i with a centered Eulerian line y_j, i.e. to be a point mass concentrated at the approximate center of mass of each IECV. To prepare for the second cascade, these concentrated masses are first notionally re-assigned from IECV's to intermediate LCV's (ILCV's) that are aligned along the centered Lagrangian lines X_i. The individual ILCV's along X_i are bounded in the Y direction by Lagrangian lines passing through points located midway between two consecutive "center-of-mass" points (denoted by solid (green) triangles) along X_i. In the X direction they are bounded by $X_{i-1/2}$ and $X_{i+1/2}$: $\Delta X_i \equiv X_{i+1/2} - X_{i-1/2}$ is constant in this Lagrangian coordinate system. Knowing the mass distribution of ILCV's, the second cascade is then performed along centered Lagrangian X_i lines to one-dimensionally remap mass (again using either PSM [22] or PPM [20]), from the assumed centers of mass of the ILCV's (solid (green) triangles) to the assumed centers of mass of the LCV's, i.e. the midpoints between the solid (blue) triangles along X_i. Here, distances along the piecewise-defined Lagrangian (dashed blue) lines X_i, for both remapping algorithms, are computed as cumulative physical distance.

2.2.4. Average densities at time t_1 on the Eulerian mesh

The masses of the LCV's at time t_0 are now known. These masses are then transported to their arrival ECV's, and the average densities at the new timestep are obtained from the mass of the LCV's and the volumes (areas) of the ECV's. Note that no knowledge of the complex 2D geometrical details of the individual Lagrangian cells is required or computed at any stage. This confers a significant efficiency advantage on the SLICE methodology over fully geometrical remapping algorithms.

2.2.5. Spherical geometry

For applications in spherical geometry, the same methodology is applied except that: (i) the Cartesian grid (x,y) is replaced by a standard latitude–longitude grid (λ, ϕ); (ii) points on the spherical grid are connected using great circle arcs; and (iii) due to the singularity of the poles, careful treatment in polar regions is required – see [19] for details.

3. Numerical examples

Standard tests from the atmospheric modelling literature for solid-body rotation and deformational flow, in both 2D Cartesian and spherical geometries, are used to assess the performance of the SLICE scheme in combination with either the PSM or PPM remappings. For simplicity, and also to focus on the comparative impact of the PSM and PPM remapping algorithms, the semi-Lagrangian trajectories (obtained by solving (2.4)) are determined analytically for all test problems as in [22,23]. In all the test problems used here, the initial and analytical solutions are obtained by simply sampling the analytical expressions at the required locations and times (i.e., assuming that the given functions are representations of $\bar{\rho}$). An alternative approach would be to assume that the given functions are representations of ρ, and then to integrate these to obtain $\bar{\rho}$. A previous study [18] found that the conclusions drawn from the results are independent of the choice of the approach as long as the schemes are compared with the same choice in a consistent manner.

To simplify nomenclature within this section, "PSM"/"PPM" signifies the use of PSM/ PPM within the SLICE framework [18] *without* their respective monotonicity filters activated: similarly for "PSM-M"/ "PPM-M" but *with* activation of their monotonicity filters – see [22,23] for details of the filter applied to PSM, and [20] for details of that applied to PPM. Thus all four SLICE schemes (denoted by PSM, PPM, PSM-M and PPM-M) differ only in their reconstruction module. Also, an entry of "0.00000" in an error table denotes zero to the given number of decimal places whereas "0" denotes a value that is identically zero.

3.1. Performance measures

Performance is measured using the same error measures as suggested by [24], namely:

$$l_1 \equiv \frac{I(|\overline{\rho}^{\text{num}} - \overline{\rho}^{\text{an}}|)}{I(|\overline{\rho}^{\text{an}}|)}, \tag{3.1}$$

Table 1
Comparative errors for solid-body rotation of a cosine hill on a plane

	l_1	l_2	l_∞	$l_{\min}$	$l_{\max}$
PSM	0.15099	0.08537	0.06128	−0.02031	−0.06128
PPM	0.24439	0.13454	0.11648	−0.03033	−0.11648
PSM-M	0.09354	0.06625	0.05455	0	−0.05205
PPM-M	0.23563	0.22557	0.34744	0	−0.34744

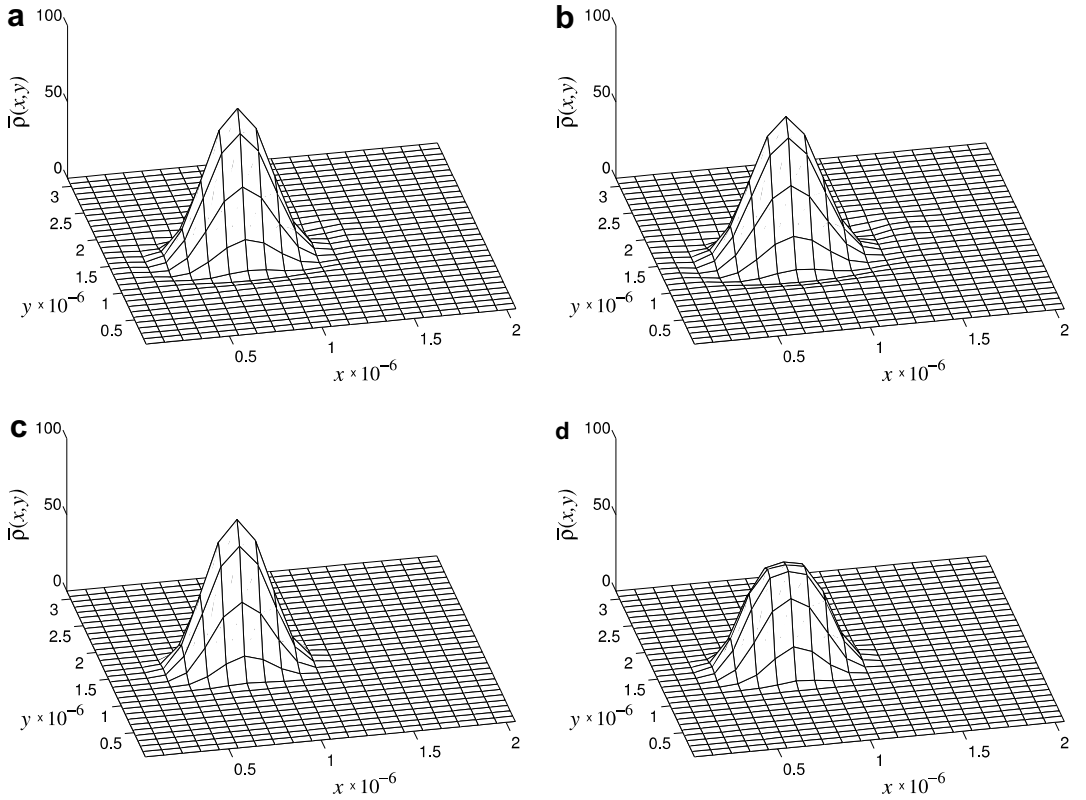

Fig. 2. Solid-body rotation of a cosine hill after 1 rotation: (a) PSM; (b) PPM; (c) PSM-M; and (d) PPM-M.

Table 2
Comparative errors for solid-body rotation of a slotted cylinder on a plane

	l_1	l_2	l_∞	$l_{\min}$	$l_{\max}$
PSM	0.19174	0.21418	0.63417	−0.13876	0.14290
PPM	0.22298	0.23625	0.65472	−0.16810	0.14915
PSM-M	0.17344	0.22175	0.67874	0	−0.00006
PPM-M	0.18723	0.23313	0.72406	0	0.00000

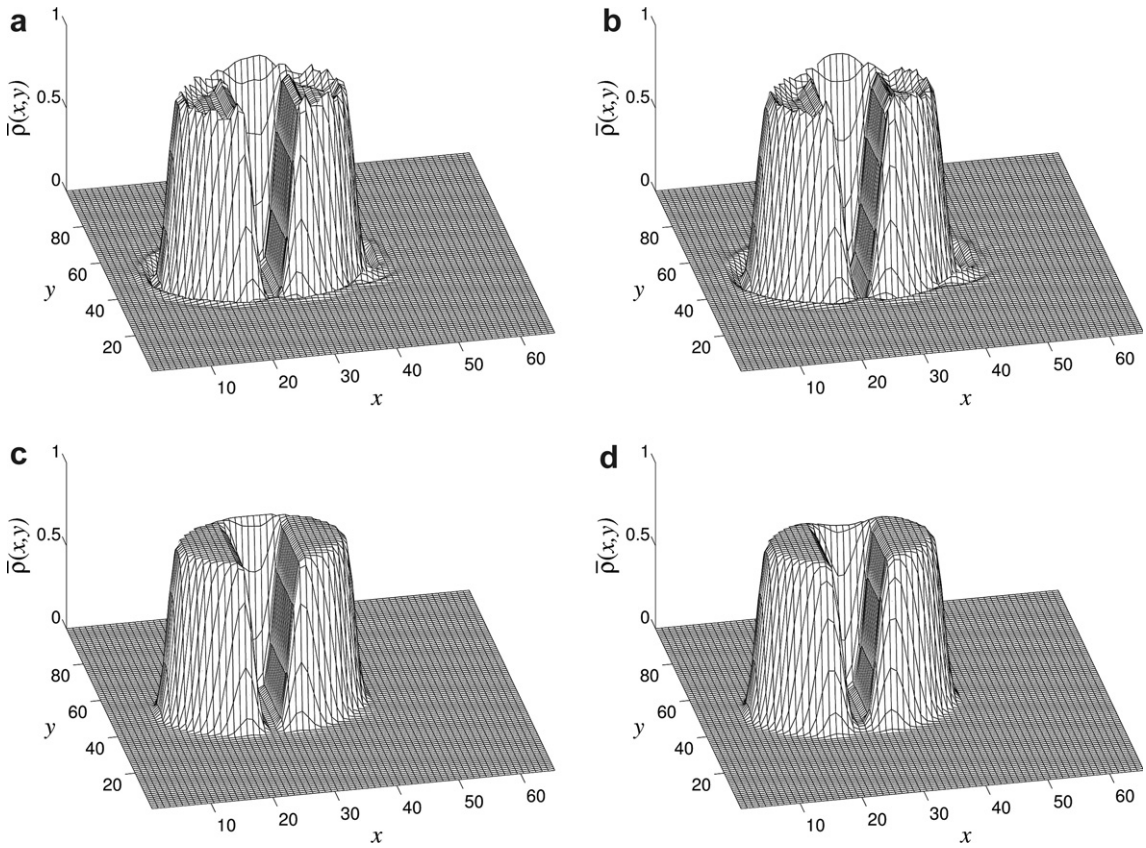

Fig. 3. Solid-body rotation of a slotted cylinder on a plane after 1 rotation: (a) PSM; (b) PPM; (c) PSM-M; and (d) PPM-M.

Table 3
Comparative errors for solid-body rotation of a cosine hill on a sphere after one rotation as a function of rotation axis: $\Delta t = \Delta t_0$ and 256 timesteps for all experiments

	l_1	l_2	l_∞	$l_{\min}$	$l_{\max}$
(a) *Cross-polar flow*: $\alpha = \pi/2$					
PSM	0.07947	0.05379	0.04874	−0.01772	−0.02593
PPM	0.10304	0.06479	0.05520	−0.03103	−0.02993
PSM-M	0.05724	0.04597	0.04256	0	−0.03320
PPM-M	0.10909	0.10182	0.11796	0	−0.11342
(b) *Equatorial flow*: $\alpha = 0$					
PSM	0.04969	0.03358	0.02689	−0.01551	−0.01352
PPM	0.06965	0.04488	0.03499	−0.02105	−0.01851
PSM-M	0.02711	0.01947	0.01792	0	−0.01792
PPM-M	0.10083	0.09538	0.11474	0	−0.11474
(c) *Diagonal flow*: $\alpha = \pi/4$					
PSM	0.05944	0.03264	0.02191	−0.01308	−0.01379
PPM	0.08305	0.04629	0.03055	−0.02018	−0.01393
PSM-M	0.02878	0.02022	0.02486	0	−0.02217
PPM-M	0.07802	0.08618	0.15918	0	−0.15718
(d) *Quasi-cross-polar flow*: $\alpha = \pi/2 - 0.05$					
PSM	0.07743	0.05216	0.04348	−0.01614	−0.02422
PPM	0.11112	0.06660	0.05031	−0.04593	−0.02805
PSM-M	0.05577	0.04472	0.04402	0	−0.02994
PPM-M	0.10871	0.10195	0.12437	0	−0.11667

$$l_2 \equiv \frac{\sqrt{I((\lceil\overline{\rho}^{\mathrm{num}} - \bar{\rho}^{\mathrm{an}}\rceil)^2)}}{\sqrt{I(\lceil\bar{\rho}^{\mathrm{an}}\rceil^2)}}, \tag{3.2}$$

$$l_\infty \equiv \frac{\max(|\bar{\rho}^{\mathrm{num}} - \bar{\rho}^{\mathrm{an}}|)}{\max(|\bar{\rho}^{\mathrm{an}}|)}, \tag{3.3}$$

$$l_{\min} \equiv \frac{\min(\bar{\rho}^{\mathrm{num}}) - \min(\bar{\rho}^{\mathrm{an}})}{\max(\bar{\rho}^{\mathrm{an}}) - \min(\bar{\rho}^{\mathrm{an}})}, \tag{3.4}$$

$$l_{\max} \equiv \frac{\max(\bar{\rho}^{\mathrm{num}}) - \max(\bar{\rho}^{\mathrm{an}})}{\max(\bar{\rho}^{\mathrm{an}}) - \min(\bar{\rho}^{\mathrm{an}})}, \tag{3.5}$$

where $\bar{\rho}^{\mathrm{num}}$ and $\bar{\rho}^{\mathrm{an}}$ refer to the numerical and analytical solutions, respectively,

$$I(\bar{\rho}) \equiv \sum_i \sum_j \bar{\rho}_{i,j} A_{i,j} \tag{3.6}$$

is a global integral (or global mass), and $\bar{\rho}_{i,j}$ is the average density at the center of $\mathrm{ECV}_{i,j}$ whose area is $A_{i,j} = (x_{i+1/2} - x_{i-1/2})(y_{j+1/2} - y_{j-1/2})$ in Cartesian geometry and $A_{i,j} = (\lambda_{i+1/2} - \lambda_{i-1/2})(\sin\phi_{j+1/2} - \sin\phi_{j-1/2})$ in spherical geometry on a sphere of unit radius.

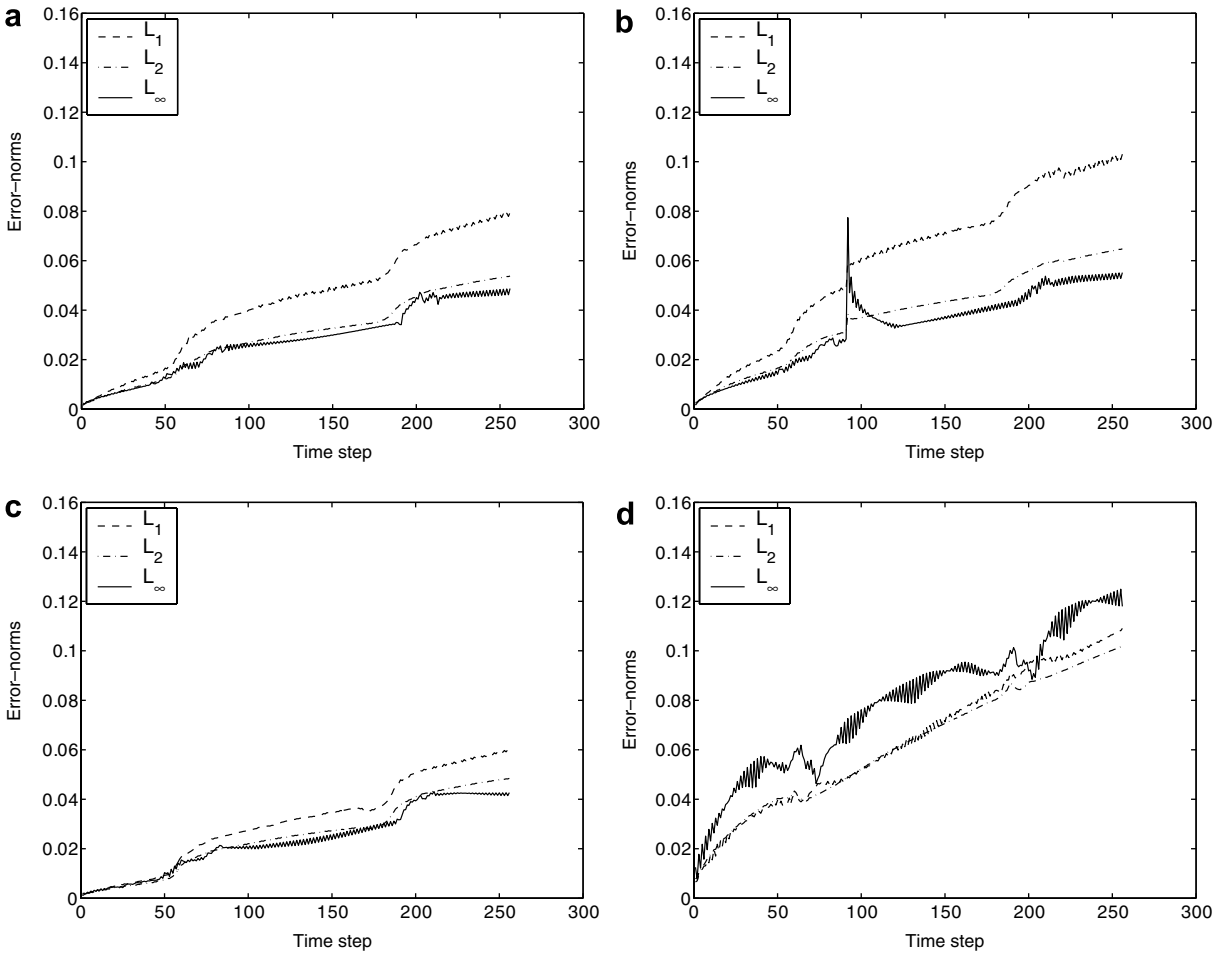

Fig. 4. Error norms versus time for solid-body rotation of a cosine hill on a sphere with a cross-polar flow ($\alpha = \pi/2$) and with $\Delta t = \Delta t_0$ using: (a) PSM, (b) PPM, (c) PSM-M and (d) PPM-M.

3.2. 2D transport on a plane

3.2.1. Solid-body rotation of a cosine hill on a plane

This is the cosine-hill problem of Section 4(c) of [18]. The parameter values are (see [18] for parameter definitions): $\Omega = [0, 32 \times 10^5 \text{ m}]^2$ (domain dimensions); $\omega = 10^{-5} \text{ s}^{-1}$ (angular velocity); $N_x = N_y = 32$ (number of ECV's in x and y directions, respectively); number of timesteps $= N_t = 71$ (1 rotation); $\Delta t = 2\pi/(\omega N_t) \simeq 8849.56$ s (timestep length); $C \simeq 2$ (maximum Courant number); $\bar{\rho}_0 = 100$ (initial maximum value); $\gamma = 8 \times 10^5$ m, $\sigma = 4 \times 10^5$ m (parameters to define the cosine hill); $(x_0, y_0) = (7.5 \times 10^5 \text{ m}, 15.5 \times 10^5 \text{ m})$ (initial location of hill center); and $(x_c, y_c) = (15.5 \times 10^5 \text{ m}, 15.5 \times 10^5 \text{ m})$ (location of center of rotation).

The errors of PSM, PPM, PSM-M and PPM-M for this problem after one rotation are summarised in Table 1, with their corresponding fields displayed in Fig. 2 over a subdomain of the full domain. It is seen from Table 1 that PSM is more accurate than PPM for all error measures, and similarly for PSM-M vs. PPM-M. In particular, PSM-M is significantly more accurate than PPM-M. PSM-M (see Fig. 2(c)) acts like a positive-definite filter to correct undershoots whilst leaving the remainder of the hill intact. However, in addition to removing undershoots in a similar manner to PSM-M, PPM-M excessively clips the hill's summit (see Fig. 2(d)). This illustrates the more discriminating behaviour of PSM's monotonicity filter in the presence of local extrema.

3.2.2. Solid-body rotation of a slotted cylinder on a plane

This is the slotted cylinder problem of Section 4(b) of [18]. The parameter values are (see [18] for parameter definitions): $\Omega = [0, 100]^2$ (computational domain); $\omega = 0.3635 \times 10^{-4} \text{ s}^{-1}$ (angular velocity); $N_x = N_y = 100$ (number of ECV's in x and y directions, respectively); number of timesteps $= 96$ (1 rotation); $\Delta t = 2\pi/(\omega N_t) \simeq 1800.55$ s (timestep length); $C \simeq 3.27$ (maximum Courant number); $\bar{\rho}_0 = 1$ (initial maximum value); $\gamma = 25$, $\sigma = 15$, $s_w = 6$, $s_l = 25$ (parameters to define the slotted cylinder); $(x_0, y_0) = (25, 50)$ (initial location of cylinder center); and $(x_c, y_c) = (50, 50)$ (location of center of rotation).

The errors of PSM, PPM, PSM-M and PPM-M for this problem after one rotation are summarised in Table 2, with their corresponding fields displayed in Fig. 3. It is seen from Table 2 that, as for the previous problem, PSM is again more accurate overall than PPM, although now by not so great a margin. Both PSM-M and PPM-M remove the spurious undershoots and overshoots that occur near cylinder edges

Table 4
As in Table 3 but Δt, and the number of timesteps per rotation, vary as indicated

	l_1	l_2	l_∞	$l_{\min}$	$l_{\max}$
(a) *Cross-polar flow*: $\alpha = \pi/2$, $\Delta t = (256/85)\Delta t_0$, *85 timesteps*					
PSM	0.04330	0.02898	0.02325	−0.01094	−0.00639
PPM	0.05306	0.03373	0.02700	−0.01369	−0.00654
PSM-M	0.03281	0.02560	0.02352	0	−0.01616
PPM-M	0.04976	0.04888	0.06181	0	−0.05460
(b) *Equatorial flow*: $\alpha = 0$, $\Delta t = (256/36)\Delta t_0$, *36 timesteps*					
PSM	0.01124	0.00890	0.00875	−0.00733	−0.00196
PPM	0.01732	0.01276	0.01148	−0.00993	−0.00231
PSM-M	0.00719	0.00666	0.01140	0	−0.01099
PPM-M	0.03278	0.03355	0.04027	0	−0.04002
(c) *Diagonal flow*: $\alpha = \pi/4$, $\Delta t = (256/64)\Delta t_0$, *64 timesteps*					
PSM	0.02055	0.01279	0.00952	−0.00754	−0.00238
PPM	0.03024	0.01792	0.01258	−0.01034	−0.00328
PSM-M	0.01246	0.00978	0.01630	0	−0.01297
PPM-M	0.03255	0.03690	0.07245	0	−0.06921
(d) *Quasi-cross-polar flow*: $\alpha = \pi/2 - 0.05$, $\Delta t = (256/17)\Delta t_0$, *17 timesteps*					
PSM	0.02394	0.01614	0.01201	−0.00679	−0.00255
PPM	0.02606	0.01721	0.01230	−0.00774	−0.00297
PSM-M	0.01978	0.01593	0.01516	0	−0.01243
PPM-M	0.02428	0.02110	0.03042	0	−0.02701

(Fig. 3). However PSM-M maintains a better defined slot than PPM-M does (cf. Fig. 3(c) with Fig. 3 (d)), particularly for its opening at the base of the cylinder and for the maintenance of the height of its rear bridge.

3.3. 2D transport on a sphere

3.3.1. Solid-body rotation of a cosine hill on a sphere

This is the cosine-hill problem of Section 3(a) of [19]. It consists of the solid-body rotation of a bell-shaped hill about an axis making an angle α with the polar axis of the sphere. The parameter values are (see [19] for

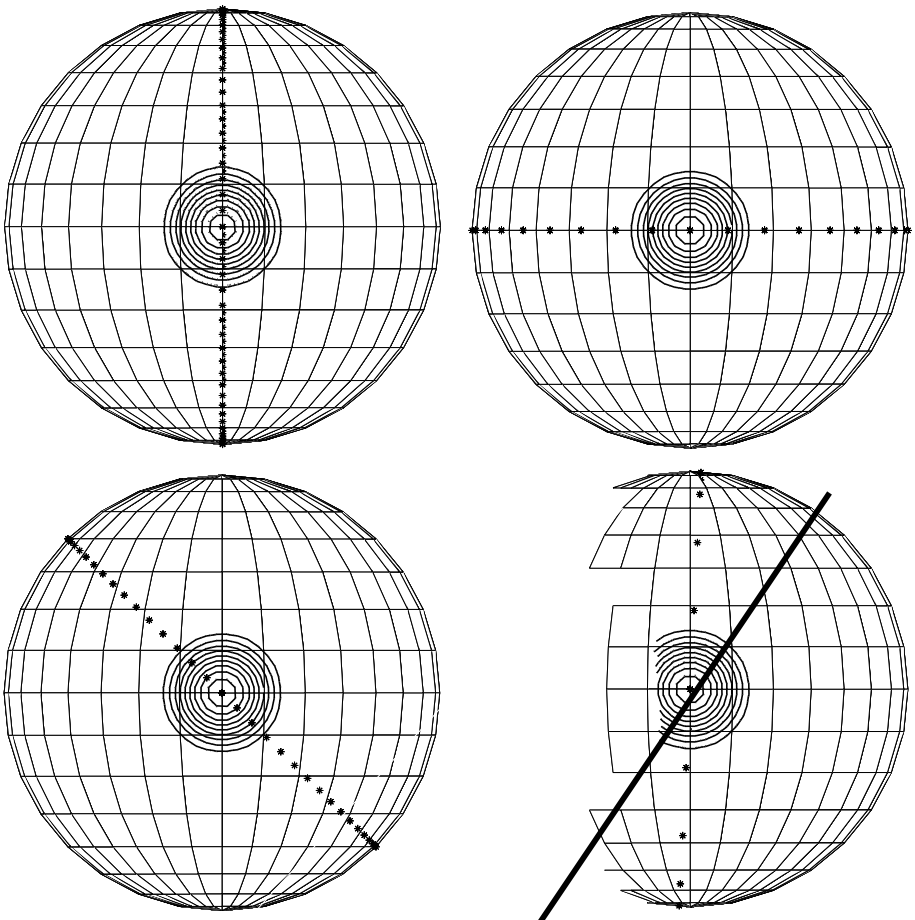

Fig. 5. Results (displayed on an orthographic projection) after one rotation with different rotational axes and various Courant numbers for solid-body rotation of a cosine hill on a sphere using PSM-M for: (a) cross-polar flow ($\alpha = \pi/2$) with $\Delta t = 256\Delta t_0/85$; (b) equatorial flow ($\alpha = 0,\ \Delta t = 256\Delta t_0/36$); (c) diagonal flow ($\alpha = \pi/4,\ \Delta t = 4\Delta t_0$); and (d) quasi-cross-polar flow ($\alpha = \pi/2 - 0.05,\ \Delta t = 256\Delta t_0/17$). PSM-M and analytical solutions shown in solid and dashed contours, respectively; time evolution of the bell center by asterisks, with one per timestep; and contour interval = 0.1 with outermost contour = 0.1.

Table 5
Comparative errors at $t = 6$ for smooth deformation of two vortices on a sphere

	l_1	l_2	l_∞	$l_{\min}$	$l_{\max}$
PSM	0.00260	0.00858	0.06354	0.00000	0.00000
PPM	0.00351	0.01174	0.08174	0.00000	0.00000
PSM-M	0.00298	0.00983	0.06406	0.00000	0.00000
PPM-M	0.00403	0.01277	0.07680	0.00015	−0.00013

parameter definitions): $N_\lambda = 128$, $N_\phi = 64$ (number of ECV's in λ and ϕ directions, respectively); $R = 7\pi/64$ (radius of the hill's base); and $(\lambda_c^0, \phi_c^0) = (\pi/2, 0)$ (position of the hill's center at initial time).

The timestep required to complete one rotation in 256 timesteps (as in [12,19,24]) is denoted by $\Delta t = \Delta t_0$, and it corresponds to a meridional Courant number of $C_\phi = 0.5$ when the wind is in the pole-to-pole direction. A series of integrations using this timestep has been performed for various rotation axes corresponding to: (a) cross-polar flow ($\alpha = \pi/2$); (b) equatorial flow ($\alpha = 0$); (c) diagonal flow ($\alpha = \pi/4$); and (d) quasi-cross-polar flow ($\alpha = \pi/2 - 0.05$). Errors after one rotation are summarised in Table 3 for these integrations. The evolution of the errors throughout the integration for the case of $\alpha = \pi/2$ is shown in Fig. 4. Consistent with the above findings for solid-body rotation of a cosine hill on a plane, it is seen that the PSM/ PSM-M results are again more accurate than the PPM/PPM-M ones for all error measures, and that PSM-M is significantly more accurate than PPM-M.

Further integrations have also been performed using the same rotation axes, but with a selection of timesteps that give zonal and meridional Courant numbers as large as $C_\lambda \equiv u\Delta t/(\Delta\lambda\cos\phi) = 64$ and $C_\phi \equiv v\Delta t/\Delta\phi = 7.5$, respectively. Errors after one rotation are summarised in Table 4 and correspond to: (a) cross-polar flow ($\alpha = \pi/2$) with $\Delta t = 256\Delta t_0/85$; (b) equatorial flow ($\alpha = 0,\ \Delta t = 256\Delta t_0/36$); (c) diagonal flow ($\alpha = \pi/4,\ \Delta t = 256\Delta t_0/64$); and (d) quasi-cross-polar flow ($\alpha = \pi/2 - 0.05,\ \Delta t = 256\Delta t_0/17$). Results for the four associated PSM-M integrations are displayed in Fig. 5. It is seen from Table 4 that the PSM/ PSM-M results are again more accurate than the PPM/PPM-M ones for all error measures. Not only are

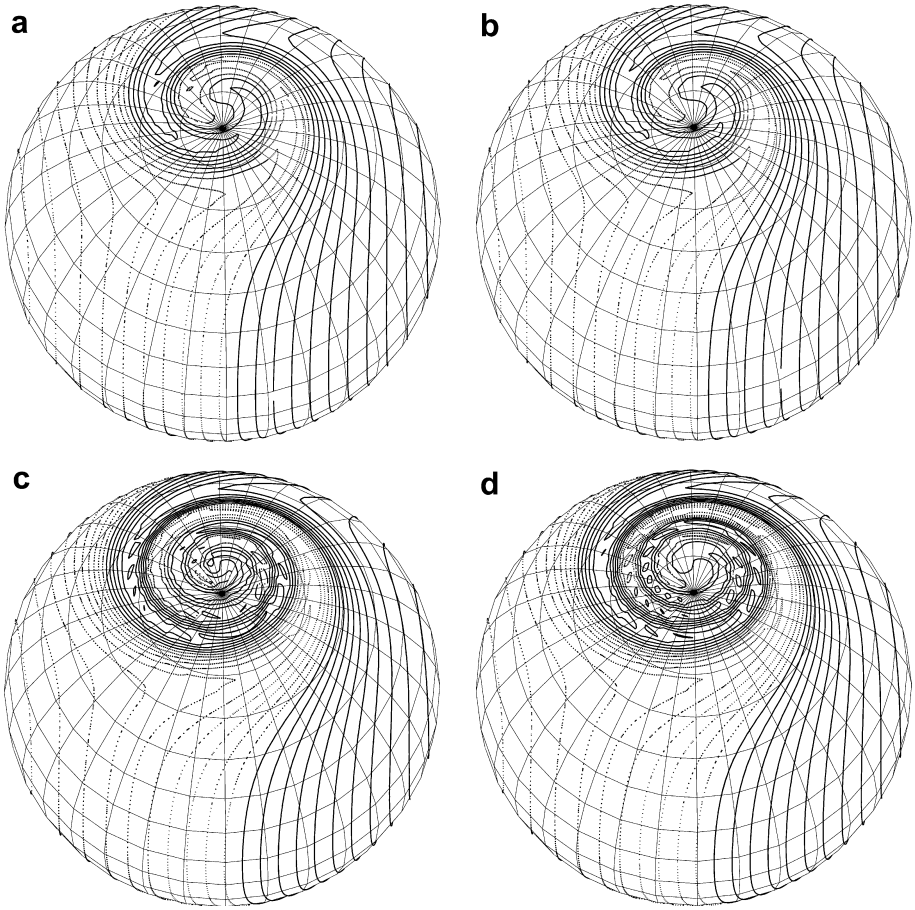

Fig. 6. Results of PSM-M at times $t = 3$ and $t = 6$ for smooth deformation of two vortices on a sphere: (a) PSM-M at $t = 3$ (64 timesteps); (b) analytic solution at $t = 3$; (c) PSM-M at $t = 6$ (128 timesteps); and (d) analytic solution at $t = 6$. All panels have 20 equally spaced contours (contour interval = 0.05) from 0.5 to 1.5 (contours are dashed when less than 1.0, and full when greater than or equal to 1.0).

all four methods stable at large Courant number, the errors are generally smaller because of reduced smoothing due to the reduced number of remappings needed to perform one rotation.

3.3.2. Smooth deformation of two vortices on a sphere

This is the generalization of Doswell's problem [25] of [11] and Section 3(b) of [19]. The parameter values are (see [19] for parameter definitions): $N_\lambda = 128$, $N_\phi = 64$ (number of ECV's in λ and ϕ directions, respectively); $\Delta t = 3/64$ (timestep); $r_0 = 3$ (radial distance); and $d = 5$ (characteristic width). The number of timesteps is $N_t = 64$ for $t = 3$ and $N_t = 128$ for $t = 6$.

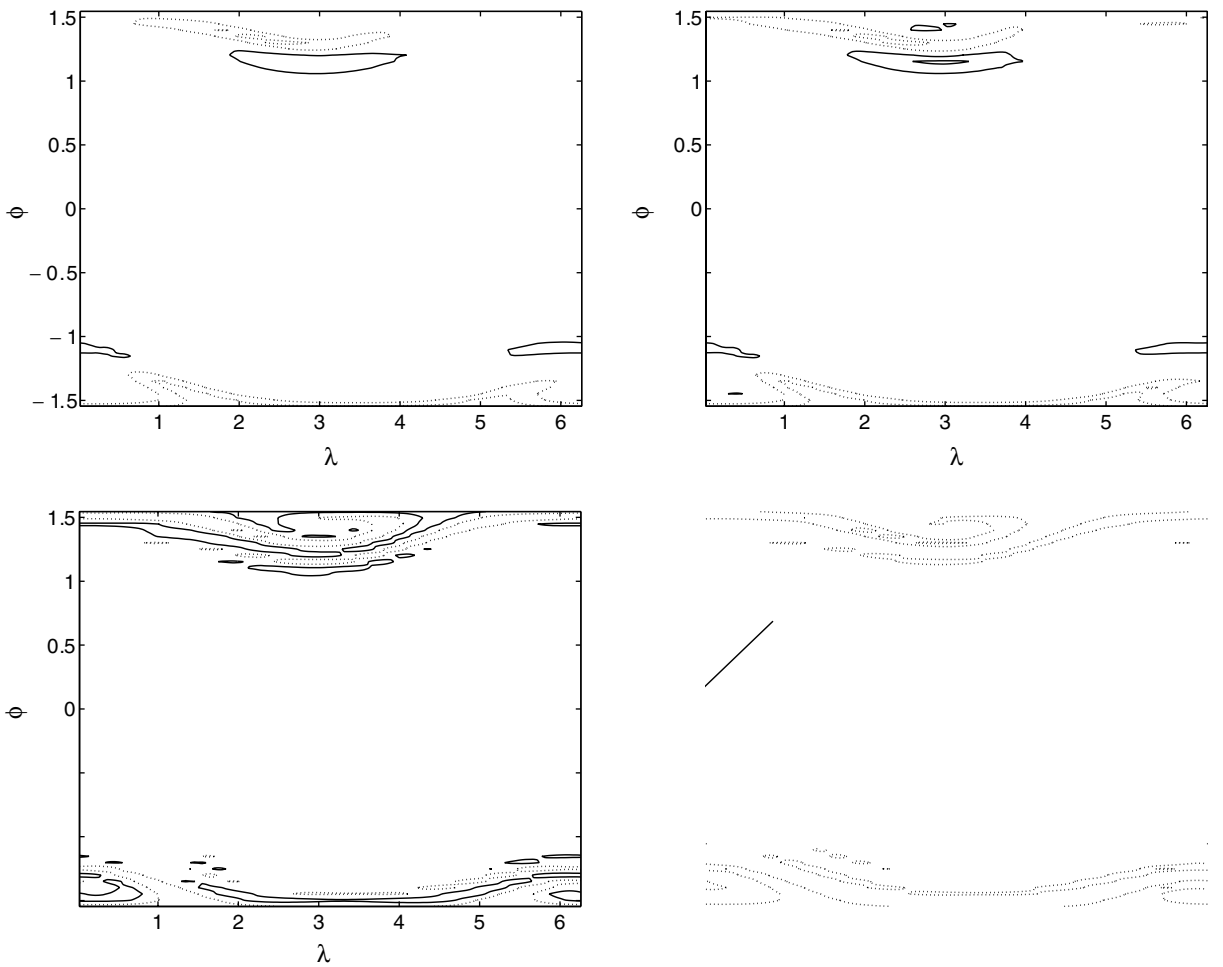

The errors of PSM, PPM, PSM-M and PPM-M for this problem at time $t = 6$ are summarised in Table 5. Examination reveals that PSM/PSM-M are again more accurate than PPM/ PPM-M for all error measures, and the effect of the monotonic filter is small due to the relative smoothness of the problem. The analytic solution, together with the PSM-M results, is displayed in Fig. 6 at times $t = 3$ and $t = 6$, with close agreement being observed between them at both times. Differences between the analytical and numerical solutions using both PSM-M and PPM-M are displayed in Fig. 7.

3.3.3. Non-smooth deformation of a vortex on a sphere

This is the non-smooth deformational flow problem of [26] and Section 3(c) of [19]. The parameter values are (see [19] for parameter definitions): $N_\lambda = 128$, $N_\phi = 64$ (number of ECV's in λ and ϕ directions, respectively); $\Delta t = 2.5/64$ (timestep): $\gamma = 3/2$ (stretching parameter), and $d = 0.01$ (characteristic width).

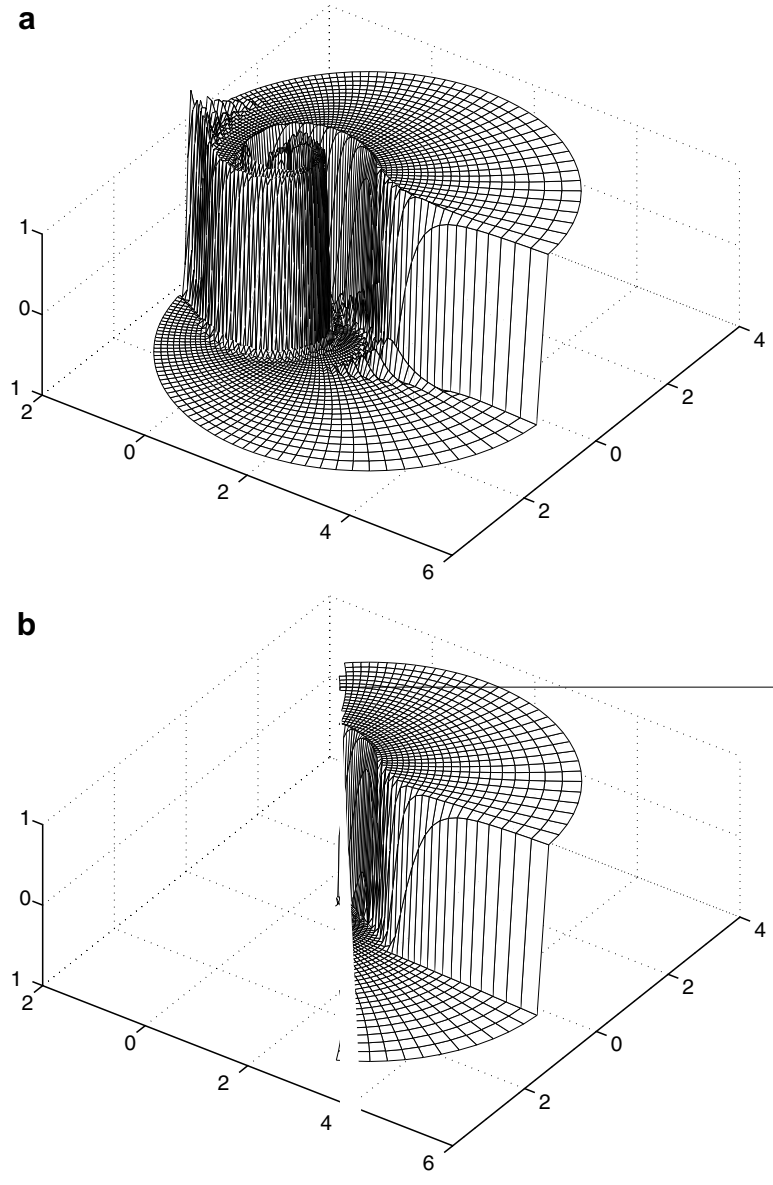

Fig. 8. Results at $t = 2.5$, projected on the plane tangent to the vortex center, for non-smooth deformation of a vortex on a sphere: (a) PSM; and (b) PSM-M.

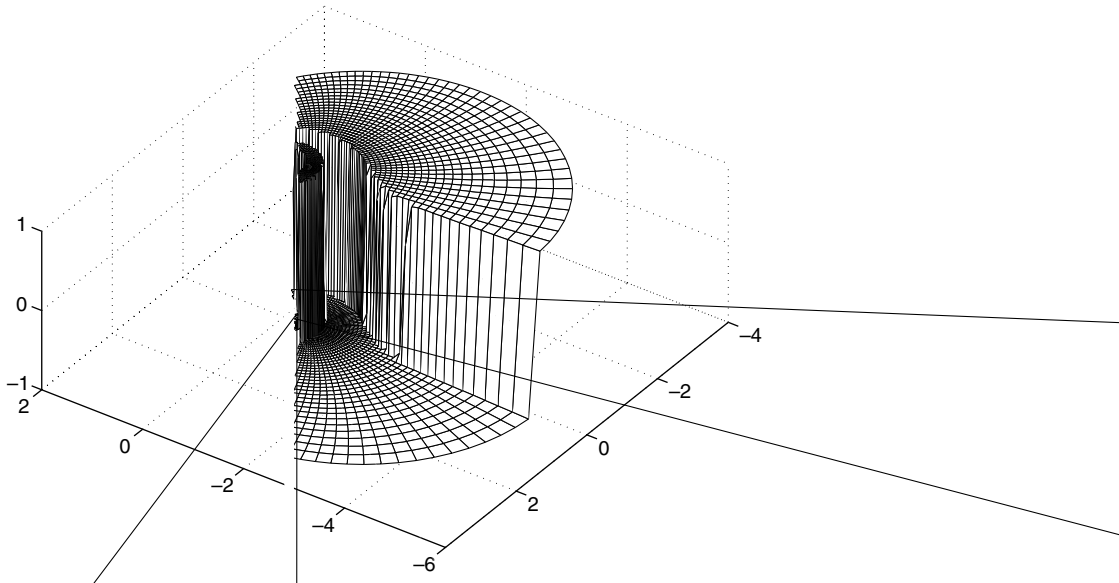

Fig. 9. As in Fig. 8, but for the analytical solution.

The errors of PSM, PPM, PSM-M and PPM-M for this problem are summarised in Table 6, and generally lead to similar conclusions as those drawn from the other problems examined. However, whilst the l_1 and l_2 errors are a bit smaller for PSM/ PSM-M when compared with those of PPM/ PPM-M, the l_∞ errors are a bit larger, as are the $l_{\min}$ and $l_{\max}$ errors for PSM-M with respect to those of PPM-M. The PSM and PSM-M solutions at $t = 2.5$, projected onto a plane tangent to the vortex center (see [26] for details), are displayed in Fig. 8 and the analytical solution in Fig. 9. It is seen that the base of the vortex wall is better defined when PSM's monotonic filter is activated.

Note that despite applying the monotonicity filter, there are still undershoots and overshoots, as evident from Table 6. This is because SLICE works by remapping the mass field. Therefore, in order that a global minimum ($\rho_{\min}$) or a global maximum ($\rho_{\max}$) of density be retained, SLICE would need to know the relationship between mass and density (i.e. the volume) when it is performing the conservative remapping steps. A crucial advantage of SLICE, in terms of computational efficiency, is that during these remapping stages it does not know the volume associated with an element of mass. Only once all the conservative remappings are complete is the density computed by dividing the mass by the Eulerian volume, which is known and invariant in time. A consequence is that, while the monotonicity filter can preserve the appropriate minima and maxima of the mass during remapping, this does not guarantee that the final density is similarly constrained.

4. Conclusions

The parabolic spline based remapping reported in [22] has been successfully combined with the SLICE flow-dependent splitting strategy for two-dimensional conservative transport problems [18,19,23]. The resulting scheme makes the possibility of higher-dimensional remapping with high-order reconstructions, without a prohibitive computational cost, a reality. To assess the performance of the present scheme in a meteorological context, standard tests in two-dimensional Cartesian and spherical geometries have been considered. Results show that: (i) SLICE with either of the PSM and PPM remappings gives good results; (ii) it does so without the need to resort to more complex and computationally expensive multi-dimensional remappings; and (iii) using the more efficient PSM remapping generally leads to more accurate results than using PPM.

A further advantage of the SLICE methodology is that its efficiency increases when applied to the transport of an increasing number of physical/chemical species, since only one set of intersection points need be computed: hence this overhead can be amortised over all species rather than just a single one.

References

[1] A. Staniforth, J. Côté, Semi-Lagrangian integration schemes for atmospheric models – a review, Mon. Weather Rev. 119 (1991) 2206–2223.
[2] S. Moorthi, R.W. Higgins, J.R. Bates, A global multilevel atmospheric model using a vector semi-Lagrangian finite-difference scheme. Part II: Version with physics, Mon. Weather Rev. 123 (1995) 1523–1541.
[3] A. Priestley, A quasi-conservative version of the semi-Lagrangian advection scheme, Mon. Weather Rev. 121 (1993) 621–629.
[4] I.M. Navon, Implementation of a posteriori methods for enforcing conservation of potential enstrophy and mass in discretized shallow-water equations models, Mon. Weather Rev. 109 (1981) 946–958.
[5] M. Rančić, An efficient conservative monotonic remapping for semi-Lagrangian transport algorithms, Mon. Weather Rev. 123 (1995) 1213–1217.
[6] J.P.R. Laprise, A. Plante, A class of semi-Lagrangian integrated mass (SLIM) numerical transport algorithms, Mon. Weather Rev. 123 (1995) 553–565.
[7] L.M. Leslie, R.J. Purser, Three-dimensional mass-conserving semi-Lagrangian scheme employing forward trajectories, Mon. Weather Rev. 123 (1995) 2551–2566.
[8] B. Machenhauer, M. Olk, On the development of a cell-integrated semi-Lagrangian shallow water model on the sphere, in: ECMWF Workshop Proceedings: Semi-Lagrangian Methods, ECMWF, Reading, UK, 1996, pp. 213–228.
[9] B. Machenhauer, M. Olk, The implementation of the semi-implicit cell-integrated semi-Lagrangian models, Atmos. Ocean 35 (1997) 103–126 (special issue).
[10] F. Xiao, T. Yabe, Completely conservative and oscillationless semi-Lagrangian schemes for advection transportation, J. Comput. Phys. 170 (2001) 498–522.
[11] R. Nair, B. Machenhauer, The mass conservative cell-integrated semi-Lagrangian advection scheme on the sphere, Mon. Weather Rev. 130 (2002) 649–667.
[12] R. Nair, J. Scroggs, F. Semazzi, Efficient conservative global transport schemes for climate and atmospheric chemistry models, Mon. Weather Rev. 130 (2002) 2059–2073.
[13] R. Nair, J. Scroggs, F. Semazzi, A forward trajectory global semi-Lagrangian transport scheme, J. Comput. Phys. 190 (2003) 275–294.
[14] R. Nair, Extension of a conservative cascade scheme on the sphere to large Courant numbers, Mon. Weather Rev. 132 (2004) 390–395.
[15] X. Peng, F. Xiao, W. Ohfuchi, H. Fuchigami, Conservative semi-Lagrangian transport on a sphere and the impact on vapor advection in an atmospheric general circulation model, Mon. Weather Rev. 133 (2005) 504–520.
[16] P.H. Lauritzen, E. Kaas, B. Machenhauer, A mass-conservative semi-implicit semi-Lagrangian limited area shallow-water model on the sphere, Mon. Weather Rev. 134 (2006) 1205–1221.
[17] P.H. Lauritzen, A stability analysis of finite-volume advection schemes permitting long time steps, Mon. Weather Rev. (in press).
[18] M. Zerroukat, N. Wood, A. Staniforth, SLICE: a semi-Lagrangian inherently conserving and efficient scheme for transport problems, Q. J. R. Meteorol. Soc. 128 (2002) 2801–2820.
[19] M. Zerroukat, N. Wood, A. Staniforth, SLICE-S: a semi-Lagrangian inherently conserving and efficient scheme for transport problems on the sphere, Q. J. R. Meteorol. Soc. 130 (2004) 2649–2664.
[20] P. Colella, P. Woodward, The piecewise parabolic method (PPM) for gas-dynamical simulations, J. Comput. Phys. 54 (1984) 174–201.
[21] R.J. Purser, L.M. Leslie, An interpolation procedure for high-order three-dimensional semi-Lagrangian models, Mon. Weather Rev. 119 (1991) 2492–2498.
[22] M. Zerroukat, N. Wood, A. Staniforth, The parabolic spline method (PSM) for conservative transport problems, Int. J. Numer. Meth. Fluid 11 (2006) 1297–1318.
[23] M. Zerroukat, N. Wood, A. Staniforth, A monotonic and positive-definite filter for a semi-Lagrangian inherently conserving and efficient (SLICE) scheme, Q. J. R. Meteorol. Soc. 131 (2005) 2923–2936.
[24] D.L. Williamson, J.B. Drake, J.J. Hack, R. Jakob, P.N. Swarztrauber, A standard test set for numerical approximations to the shallow-water equations in spherical geometry, J. Comput. Phys. 102 (1992) 221–224.
[25] C.A. Doswell, A kinematic analysis of frontogenesis associated with a nondivergent vortex, J. Atmos. Sci. 41 (1984) 1242–1248.
[26] R. Nair, J. Côté, A. Staniforth, Cascade interpolation for semi-Lagrangian advection over the sphere, Q. J. R. Meteorol. Soc. 125 (1999) 1445–1468.